Soft Matter

Accepted Manuscript

ROYAL SOCIETY OF CHEMISTRY

www.rsc.org/softmatter

Clostridium perfringens α-toxin interaction with red cells and model membranes

Authors: S. A. Jewell[1], R. W. Titball[2], J. Huyet[3], C. E. Naylor[3], A. K. Basak[3], P. Gologan[1], C. P. Winlove[1], P. G. Petrov[1]*

Address: (1) School of Physics, University of Exeter, Exeter, UK

(2) School of Biosciences, University of Exeter, Exeter, UK

(3) Department of Crystallography, Birkbeck College, London, UK

*Corresponding author: Dr Peter G. Petrov
School of Physics
University of Exeter
Stocker Road
Exeter
EX4 4QL
UK

Email: p.g.petrov@exeter.ac.uk

Phone: +44 (0)1392 724139

Abstract

The effects of *Clostridium perfringens* α-toxin on host cells have previously been studied extensively but the biophysical processes associated with toxicity are poorly understood. The work reported here shows that the initial interaction between the toxin and lipid membrane leads to measurable changes in the physical properties and morphology of the membrane. A Langmuir monolayer technique was used to assess the response of different lipid species to toxin. Sphingomyelin and unsaturated phosphatidylcholine showed the highest susceptibility to toxin lypolitic action, with a two stage response to the toxin (an initial, rapid hydrolysis stage followed by the insertion and/or reorganisation of material in the monolayer). Fluorescence confocal microscopy on unsaturated phosphatidylcholine vesicles shows that the toxin initially aggregates at discrete sites followed by the formation of localised "droplets" accumulating the hydrolysis products. This process is accompanied by local increases in the membrane dipole potential by about 50 ($\pm$42) mV. In contrast, red blood cells incubated with the toxin suffered a decrease of the membrane dipole potential by 50 ($\pm$40) mV in areas of high toxin activity (equivalent to a change in electric field strength of 10^7 Vm^{-1}) which is sufficient to affect the functioning of the cell membrane. Changes in erythrocyte morphology caused by the toxin are presented, and the early stages of interaction between toxin and membrane are characterised using thermal shape fluctuation analysis of red cells which revealed two distinct regimes of membrane-toxin interaction.

Keywords:

Clostridium perfringens α-toxin, lipid membrane, membrane dipole potential, erythrocyte morphology.

1. Introduction

Many bacterial toxins interact directly with host cell membranes, disrupting their integrity and triggering cascades which lead to a number of events ranging from the release of mediators of inflammation to the death of the target cell. For many infections these toxins play major roles in disease and interventions that block the activity of the toxin can prevent the development of disease. The biochemical basis of toxicity is now well understood for many of these toxins. However, there is little understanding how the biophysical properties of the target cell membrane influence the ability of the toxin to interact with the membrane. The physical properties of the cell membrane are vital to many of its functions and understanding their role in determining membrane interactions with toxins and the changes produced by toxins should provide new approaches to the diagnosis and treatment of disease.

FIGURE 1

Figure 1. α-toxin drawn as cartoon and coloured by the distance from the plane containing bound zinc and calcium ions (red into membrane, blue away from it). Exposed hydrophobic chains postulated to intercalate with hydrocarbon chains (F334, W214 and W217) are shown as sticks. The three zinc ions required for activity are shown in dark blue and the C-terminal calcium ions associated with the membrane binding are shown in lighter blue. 1,2-hexyl-phosphatidylcholine shown as spheres is modelled into the α-toxin active site by homology with its complex with *Bacillus cereus* PLC (PDBID 1P6D). The lipid bilayer (1-palmitoyl-2-oleoylphosphatidylcholine:cholesterol in 9:1 ratio) was generated using CHARMM-GUI[1] and is drawn as a semi-transparent surface. Figure drawn with PyMol[2].

Clostridium perfringens is an anaerobic bacterium associated with gas gangrene, a disease of humans and mammals that results in extensive tissue damage and which is usually fatal if left untreated. The α-toxin produced by the bacterium plays a key role in disease by modulating the host immune response to infection, promoting anoxia in host tissues and inducing the production of inflammatory mediators[3]. The toxin is a 370-residue zinc metalloenzyme that can bind to host cell membranes in the presence of calcium ions. Crystallographic studies have revealed that the enzyme is a two-domain protein[4] (Figure 1). The intoxification pathway involves the toxin binding to the phospholipid bilayer via its C-terminal domain, followed by hydrolysis by the catalytic N-domain of unsaturated membrane phosphatidylcholine (PC) and sphingomyelin (SM) to produce diacylglycerol (DAG) and ceramide. DAG is a powerful secondary messenger and its production stimulates signal transduction pathways[5-8]. This mechanism implies two types of phospholipid-binding site: an initial binding site or sites in the C-terminal domain which mediate(s) attachment (and insertion) of the toxin onto the lipid bilayer. This binding site may not be specific, but there is also an active site in the N-terminal domain which orientates a specific phospholipid for hydrolysis. The toxin activity in model lipid bilayers can be enhanced by the addition of lipids such as cholesterol which are not substrates for the enzyme[9]. This enhancement is presumably associated with the initial binding to the lipid bilayer in the C-terminal domain. This work has also revealed that the shape of the lipid molecules (and subsequently the lipid packing) is an important factor in determining the binding of the toxin with the target cell membrane. The biophysical factors contributing to the process were further illustrated by studies on large unilamellar vesicles examining the rate of enzymatic activity through its effect on solution turbidity[10, 11]. Recent studies have also imaged the phase transformations induced during initial toxin/vesicle interactions[12-14]. Though this measurement is difficult to interpret the results suggest that initially the enzyme works at a low rate until a critical amount of DAG has been produced, at which point the enzyme activity significantly increases. This phenomenon is thought to be due to the generation of localised defects and phase-separated patches created by the DAG product which allow the enzyme activity to increase. One aim of the present work was to investigate the interaction of α-toxin with lipid monolayers spread at the air-water interface on a Langmuir trough. Such systems provide insights into the interactions of specific lipid systems at well-defined packing densities making it possible to distinguish the processes of insertion and lipolysis.

Another aim of the research was to investigate the relationships between the charge structure of the membrane and toxin interactions. An important aspect of this structure is the membrane dipole potential, ψ_d, which is an electrical potential between the lipid headgroups and the hydrophobic membrane interior of the lipid bilayer of several hundred millivolts in magnitude[15] and is linked to many processes such as ion channel activation and mechanotransduction[16, 17]. The potential arises due to the polar nature of the lipid molecules and their packing density within the membrane, with contributions from the water structure at the cell surface. For a constant dielectric permittivity the dipole potential is directly proportional to the lipid packing density, which is dependent on properties such as the nature of the lipid head group and saturation of the aliphatic tail[15]. It is therefore probable that toxin interactions will have an effect on ψ_d and, conversely, ψ_d may be a determinant of membrane susceptibility to toxins. The membrane dipole potential can be measured by inserting an environmentally sensitive dye such as Di-8-ANEPPS into the lipid membrane. Such dyes have a fluorescence spectrum which is modified by the electrical environment of the surrounding molecules[18] whilst being insensitive to other electrical contributions such as surface and transmembrane potentials. Ratiometric fluorescence imaging of labelled membranes allows ψ_d to be quantified, independent of the dye concentration and bleaching effects. Measurements are reported first on giant unilamellar lipid vesicles, and then on red cells labelled with Di-8-ANEPPS. Fluorescently labelled α-toxin has been used in conjunction with these vesicles to identify sites of enzyme activity. Finally, the effect of the toxin on erythrocyte morphology has been determined by optical density measurements and thermal fluctuation spectroscopy which can be used to detect interactions between solutes and soft membranes through changes in the membrane differential area.

2. Experimental

2.1 C. perfringens α-toxin production and labelling

2.1.1 Protein expression and purification

α-toxin derived from the CER89L43 strain of *C. perfringens* was expressed in the JM105 *E. coli* strain for 16 hours at 37°C in the presence of 0.5 mM $ZnCl_2$ and 1 mM $CaCl_2$. Proteins were then extracted by the method of periplasmic extraction using 0.58 M sucrose in 20 mM Hepes, pH 8.0. α-toxin was purified by two steps anion exchange chromatography using a Q Sepharose column, followed by a Resource Q column both in 20 mM Hepes, pH 8.0 in the presence of 150 μM $ZnCl_2$ and $CaCl_2$. The protein has subsequently been purified by size exclusion chromatography using a gel filtration column (Superdex S200) in the same buffer supplemented with 150 mM NaCl. The enzymatic activity of α-toxin has been systematically checked through its ability to hydrolyse *p*-nitrophenolphosphoryl choline[19]. All experiments were performed with toxin prepared using the same protocol in order to minimise the possibility of interaction of different contaminants with the lipid membranes.

2.1.2 Protein labelling

α-toxin was chemically labelled on its sole cysteine residue (169) using Alexa-Fluor 488 (Molecular Probes). Cysteine 169 is both on the protein surface and distant from the active site and membrane-interaction surface, and was therefore not expected to affect the enzyme's folding or activity. After purification α-toxin was concentrated between 50 and 100 μM. Protein and label were mixed in a 1:15 molar ratio, in 20 mM Hepes, pH 8.0, and stirred at room temperature for 2 hours. Unconjugated label was removed by size exclusion chromatography with Superdex S200 column. Unstained SDS electrophoresis gels of the labelled toxin were scanned at 488 nm on a FujiMax fluorescence imager to confirm that the toxin was the major source of fluorescence signal. The procedure resulted in 80-90 % of cysteine residues being modified, as assessed by absorbance. Retention of the enzymatic activity of the toxin (data not shown) was confirmed by measuring hydrolysis of *p*-nitrophenolphosphoryl choline[19].

2.2 Lipid monolayer studies

Monolayers of selected lipids were prepared in a Langmuir trough modified from a commercial system (Kibron MicroTrough S). The lipid species selected for the study were 1,2-dioleoyl-sn-glycero-3-phosphocholine (DOPC), 1,2-dipalmitoyl-sn-glycero-3-phosphocholine (DPPC), a 1:1 mixture of 18:0 phosphatidylserine and 18:1 phosphatidylserine (PS) (Avanti Polar Lipids, USA) and sphingomyelin (from bovine brain, a mixture of saturated and unsaturated chains) (SM) (Sigma-Aldrich, UK). Two separate mixtures of lipids found in the red blood cell inner and outer leaflets at physiologically relevant headgroup ratios were also investigated (Table 1). These mixtures were primarily chosen to explore the effect of the lipid headgroups (therefore the chains were kept saturated) and were purchased from Avanti Polar Lipids, USA. For each study, the trough was filled with 60 ml nanopure water containing 5 mM $CaCl_2$ producing a meniscus bounded by the trough walls and two movable polytetrafluoroethylene (PTFE) barriers. 1 µl of lipid in chloroform (concentration 10 mg ml^{-1}) was added to the surface and the barrier separation was adjusted to produce a surface pressure of 30 mN m^{-1} and then left for one hour to reach equilibrium. Pressure versus area data were collected from the lipid monolayer before returning the barriers to a position producing a surface pressure of 30 mN m^{-1}. 10 µl of 0.03 mg ml^{-1} α-toxin was carefully added to the subphase, which contained a magnetic stirrer to provide rapid mixing of toxin in the subphase, bringing the toxin concentration in the subphase to $\approx$ 0.12 nM. The surface pressure was then recorded over the course of one hour. Pressure versus area data was then recorded over several compression and relaxation cycles and compared to the results obtained prior to the addition of the toxin to allow changes to the lipid monolayer to be determined.

Red blood cell inner leaflet mixture

Lipid	Percentage
16:0 PC	12
16:0 PE	38
16:0 PS	22
cholesterol	20
16:0 sphingomyelin	8

Red blood cell outer leaflet mixture

Lipid	Percentage
16:0 PC	31
16:0 PE	9
16:0 PS	1
Cholesterol	20
16:0 sphingomyelin	39

Table 1 – Lipid composition of human red blood cell leaflet mixtures used for Langmuir trough monolayer measurements (Avanti Polar Lipids, USA).

2.3 Giant unilamellar vesicle (GUV) studies

2.3.1 Electroformation of GUVs

Lipid vesicles were formed using an electroforming method modified from an approach by Angelova and Dimitrov[20]. 10 µl of the unsaturated lipid DOPC dissolved in chloroform at a concentration of 10 mg ml^{-1} was spread onto a clean piece of Indium-tin oxide (ITO) coated plastic (Sigma, resistivity 100 Ω sq^{-1}) forming a patch approximately 20 mm x 20 mm and left to dry under vacuum for two hours. An annular PTFE spacer of internal diameter 15 mm and thickness 4 mm was placed onto the dried lipid patch and a second piece of ITO coated plastic was placed on top of the spacer with the ITO surface facing inwards and the construction was clamped together to form a tight seal around the edges of the spacer. A swelling solution of 200 mM sucrose in nanopure water was injected into the central void of the annulus through one of two small holes drilled in the side of the PTFE spacer, completely filling the chamber. Electrodes were attached to the ITO plates and the assembly was placed in an incubator maintained at 37°C with the lipid coated plate lowermost. A square wave of frequency 10 Hz and r.m.s. amplitude of 1.5 V was applied across the chamber for 1 hour, the waveform was then changed to a 1.2 V sinusoidal voltage at 4 Hz for 30 minutes, with the frequency then reduced to 2 Hz for 15 minutes and finally 1 Hz for 15 minutes. The chamber was removed from the incubator and allowed to cool to room temperature before the plates were carefully separated and the vesicle-rich sucrose solution was extracted using a pipette. Prior to measurements being made the vesicle suspension was diluted 1:1 using a glucose solution of equal molarity which also contained 10 mM $CaCl_2$ producing a final Ca^{2+} concentration of 5 mM. (The $CaCl_2$ could not be included in the original sucrose solution used to swell the vesicles due to the adverse effect of the ions on the electroformation process. However, the difference in calcium concentration inside and outside the vesicles did not appear to affect the vesicle stability.)

2.3.2 Measurement of the interaction of alexa-488 labelled α-toxin with DOPC vesicles

25 µl of a DOPC vesicle/sucrose suspension was mixed with 25 µl of 200 mM glucose solution containing 10 mM $CaCl_2$ and 5 µl of 0.03 mg ml^{-1} alexa-488 labelled α-toxin in Tris–HCl buffer containing 5 mM $CaCl_2$ (producing a toxin concentration of $\approx$ 64 nM). All mixing solutions were osmotically matched and thermally equilibrated to avoid osmotic or thermal shocks to the vesicles. The solution was immediately transferred to a microscope imaging chamber constructed for fluorescence confocal microscopy as described below.

2.3.3 Measurement of the effect of α-toxin on membrane dipole potential of DOPC vesicles

25 µl of the DOPC vesicle/sucrose suspension was mixed with 25 µl of 200 mM (osmotically matched) glucose solution containing 10 mM $CaCl_2$. 0.5 µl of 1 mg ml^{-1} Di-8-ANEPPS (Sigma Alrdrich, UK) in ethanol was added to the mixture and the solution was left at 37°C for one hour. 5 µl of 0.03 mg ml^{-1} α-toxin in Tris–HCl buffer containing 5 mM $CaCl_2$ was then added to the vesicle suspension and the solution was immediately transferred to a glass microscopy chamber for imaging.

2.4 Di-8-ANEPPS labelling of red blood cells

A 5 µl sample of red blood cells was collected from a healthy volunteer using a finger-stick procedure and suspended in 1 ml of 10 mM Tris-HCl buffer containing 5 mM $CaCl_2$ and 150 mM NaCl. 5 µl of 1 mg ml^{-1} Di-8-ANEPPS in ethanol was added and the sample was left to incubate at 37°C for 2 hours. The cells were washed several times to remove the excess dye and the re-suspended in 1 ml of the buffer solution. 2 µl of 0.03 mg ml^{-1} α-toxin was added to the sample (producing a toxin concentration of $\approx$ 1.4 nM) and then immediately transferred to a microscopy imaging chamber.

2.5 Optical imaging techniques

For all optical imaging procedures, glass imaging chambers were constructed using two layers of Parafilm (Pechiney Plastic Packaging, USA) to separate a microscope slide and a coverslip and annealing on a hotplate for 15 seconds to create either a 2- or a 3-sided chamber suitable for microscopy use.

2.5.1 Ratiometric fluorescence imaging of Di-8-ANEPPS labelled material

Ratiometric imaging was performed using an Olympus IX50 inverted microscope with a 63x oil immersion lens. Excitation light was provided by a Till Photonics Polychrome V monochromator and images were collected using a low-light CCD camera (AVT Stingray F-145B) in conjunction with a 650/50 nm emission filter (Thorlabs). Images produced using excitation light of 420 nm and then 520 nm were recorded sequentially using an exposure time of 500 ms for each wavelength with a delay of $\approx$ 5 ms between the two exposures. For each image the background intensity was subtracted from the data and the resulting image was stored as a matrix of absolute intensity values. The 420 nm excitation image was then divided by the 520 nm excitation image to produce a matrix of the ratiometric intensity, $R = I_{420}/I_{520}$.

2.5.2 Confocal microscopy imaging

Confocal fluorescence images were obtained using a Leica SPF5 confocal microscope. For studies involving the Alexa-488 fluorophore excitation light was provided by the 488 nm line of an Argon-ion laser and emitted light at wavelengths above 510 nm was collected. For samples labelled with Di-8-ANEPPS the 488 nm laser line was also used but the emission wavelengths above 550 nm were collected.

2.5.3 Measurement of cell size and shape from haemoglobin absorption measurements

The transmission of 415 nm light through a sample of unlabelled red blood cells in an imaging chamber was recorded at 30 s intervals using an Olympus IX50 inverted microscope with a 63x oil immersion lens and Stingray CCD camera. Image analysis was performed using ImageJ software[21] to calculate the mean background intensity of the 415 nm light to allow the relative absorption of light by the cell at each pixel to be calculated.

2.5.4. Membrane shape and thermal fluctuation analysis

Phase contrast video microscopy (Leica DMLFS upright microscope, 63× PL FLUOTAR objective) was used to assess the thermal fluctuation dynamics and the instantaneous and mean shapes of 2D equatorial contours of individual RBCs, as described in details in[22, 23]. Video sequences (~ 40 s) of fluctuating RBCs were recorded at a frame rate of about 60 fps, and each frame was analysed to obtain a series of 2D equatorial contours of sub-pixel resolution (see Figure 2 for a snapshot). Each contour in the series was represented, using polar coordinates (r, θ), by a Fourier series[24, 25] according to

$$r(\theta) = R\left\{1 + \sum_n [a_n \cos(n\theta) + b_n \sin(n\theta)]\right\} \qquad \text{(Eq.1)}$$

The time series of the Fourier amplitudes a_n and b_n (along with the modulus $c_n = \sqrt{a_n^2 + b_n^2}$) can be used to characterise instantaneous and mean contour shapes as well as shape fluctuations around the mean[25]. We used this technique to monitor and quantify the response of the RBC to α-toxin.

FIGURE 2

Figure 2. Snapshot of a RBC in phase contrast (radius ~4 μm). The thin white line is the automatically traced equatorial contour.

For these experiments, a 5 μl sample of fresh blood was collected from a healthy volunteer by a pin-prick lancet, and suspended in 1 ml of phosphate buffer saline (pH 7.4 and osmolarity of 290 mOsm) containing 5 mM $CaCl_2$ and 1 mg ml^{-1} bovine serum albumin (Sigma Alrdrich, UK) which ensured the preservation of the RBC shape. A small volume of this suspension was introduced in an open-sided observation chamber which was subsequently mounted under the phase-contrast microscope, and the cells were allowed to settle. The 2-sided chamber allowed for the exchange of the original buffer solution with a buffer solution containing α-toxin of concentration 0.18 nM (lower than in the ratiometric study to ensure that the interactions progressed at a suitable rate for multiple fluctuation measurements to be made as well as to allow the analysis of the initial stages of interaction). This was performed by placing excess solution to one of the open sides of the chamber and drawing it through the chamber by means of filter paper placed at the opposite open side[23]. To ensure full exchange of the solution, 1 ml of toxin-containing buffer was slowly passed through the chamber. This procedure took about 5 min. Video sequences of individual cells were recorded prior to introduction of toxin, and then at regular intervals after buffer exchange for a period of up to 1 hour.

In all cases the studies were repeated several times and the results reported here represent a typical and representative behaviour.

3. Results and Discussion

3.1 Toxin activity in lipid monolayers is influenced by lipid species

The influence of the lipid properties on the interaction of the toxin with the monolayer can be observed by continuously monitoring of the surface pressure of the lipid monolayer. For all of the lipid monolayer studies reported here an α-toxin concentration in the aqueous subphase of 14 ng ml^{-1} was used and lipid monolayer area was similar in all experiments on the surface of the trough. The monolayer systems studied showed a reproducible behaviour when toxin was introduced in the aqueous phase beneath the lipid layer. Each experiment was repeated at least three times and a typical selection of results is presented below.

For each study an initial surface pressure of 30 mN m^{-1} was chosen, comparable to that in a cell membrane[26]. The time-course of change in surface pressure arising during the interaction of the toxin with the PC lipid monolayers is shown in Figure 3A for DOPC and DPPC. For the saturated lipid there is a small and steady increase of around 1 mN m^{-1} in the surface pressure over the course of 30 minutes, probably due to the C-domain of the toxin molecules inserting into the monolayer over time (but not hydrolysing the lipids). Conversely, the unsaturated PC monolayer exhibits a rapid decrease in surface pressure of 13.5 mN m^{-1} during the first 13 minutes, which can be attributed to the cleavage of the fatty acid chains during lipid hydrolysis, before showing a 3 mN m^{-1} *increase* in surface pressure over the remaining 17 minutes of the incubation period. This rise in pressure is likely to be due to molecules (either the PLC α-toxin or the DAG products from the lipid cleavage) inserting into the monolayer and/or rearrangement of the products of hydrolysis.

Figure 3B shows similar data for the 18:0/18:1 PS mixture, neither of which are substrate lipids for the toxin. In a similar way to the saturated PC, a small and steady increase in surface pressure occurs after about 5 minutes of the toxin being added to the subphase and continues throughout the incubation period. This suggests again that the toxin is inserting into the monolayer, but is unable to cleave the phospholipid, and effectively increases the lipid packing and hence surface pressure.

For SM, a substrate lipid, there is a steady decrease in pressure during the incubation process, with the surface pressure immediately and rapidly dropping at a rate of 120 mN m^{-1} per hour which is fast compared to the slow initial build up to the interaction of the toxin with DOPC. After this rapid decrease, the pressure again shows the increase associated with the ceramide products and/or toxin inserting into the membrane.

Data for inner and outer leaflet mixtures are shown in Figure 3B. In both cases surface pressure drops at an initial rate of 18 mN m^{-1} per hour during the first 10 minutes and then the inner leaflet mix settles down to an approximately linear decrease of 2 mN m^{-1} per hour after this point, and the outer leaflet mixture, 4 mN m^{-1} per hour. These rate-changes may be due to a combination of the pressure increasing again due to the toxin inserting into the monolayer, counteracting the decrease in area arising from the hydrolysis of the lipids. Despite neither leaflet mixture containing unsaturated lipids, the toxin is still able to interact with the monolayer. This most probably is due to the presence of SM in both mixtures, since the toxin shows a strong enzymatic activity for this lipid (and, presumably, at least some of the saturated SM also suffers hydrolysis), see Figure 3B. This is further confirmed by the rate of interaction with the outer leaflet mixture (containing a higher concentration of SM) which was greater than that of the inner leaflet (which contained a lower SM concentration).

FIGURE 3

Figure 3. Variation of surface pressure with time for lipid monolayers held at a constant area during a 1 hour exposure to α-toxin for (A) DOPC and DPPC, and (B) different lipid species.

3.2 Pressure-area isotherms in the presence of α-toxin

Pressure-area isotherms for the two PCs (DOPC and DPPC) are shown in Figs 4A,B. For the saturated lipid the isotherms before and after exposure to toxin were very similar, indicating that there is no significant insertion of the toxin into the monolayer even at low surface coverage. However, for the unsaturated PC the curve is displaced to the left after toxin exposure. This is consistent with the time-course data above (Figure 3A) in demonstrating that the toxin exposure results in a loss of surface-active material. It is clear that neither the toxin itself nor the degradation products could compensate for the loss of monolayer material. In addition, post-toxin the data exhibits a change in slope during the compression/relaxation cycle indicating a change in phase or structure of the monolayer within the plateau region (at $\approx$ 25 mN m^{-1}). This suggests that material such as the toxin or DAG products are being expelled from the monolayer during compression and reinserting during the relaxation phase, and similar processes have been observed in other lipid systems[27, 28]. The results shown in Figure 4A,B agree well with those in Figure 3A which clearly demonstrate the difference in toxin activity for these two types of PC monolayers.

PS is a lipid known to exert an inhibitory effect on the α-toxin activity[9], which has been attributed to the combination of a negative net charge and a positive intrinsic curvature of the lipid molecule. This is confirmed by analysing the effect of the toxin on a monolayer of phosphatidylserine (PS). Data obtained from a monolayer composed of a 1:1 mixture of PS (18:0) and PS (18:1) is shown in Figure 4C. No significant change in shape was observed in the pressure-area isotherm before and after exposure to toxin. A small shift of the curve to the right after exposure to the toxin suggests that the toxin is inserting into the membrane but is not cleaving the phospholipid, in agreement to the results shown in Figure 3B. This is in contrast with the shift seen in Figure 4D between the pre- and post-toxin measurements when it is added to a monolayer of SM. For SM monolayers, unlike the case of the DOPC monolayer, there is no evidence from the shape of the compression isotherm of toxin or hydrolysis products being expelled during the compression-relaxation cycle performed at the end of the toxin exposure (cf Figures 4B and 4D).

FIGURE 4

Figure 4. Pressure versus area isotherms for lipid monolayers before (blue dotted line) and one hour after (red solid line) the introduction of α-toxin into the aqueous subphase. The lipids used are (A) DPPC; (B) DOPC; (C) PS (18:0)/PS (18:1) and (D) SM. In all cases the trough area is in arbitrary units.

3.3 Exposure of lipid vesicles to toxin results in focal accumulation of lipid products

Giant unilamellar vesicles (GUVs) provide a simple model of the cell membrane with a surface pressure, lipid packing density and curvature comparable to that in living cells. Incubating GUVs with the bacterial toxin allows the initial interaction between the toxin and lipid bilayer to be examined without the observations being modified by secondary processes. The vesicles were all formed from DOPC, a preferred substrate for the α-toxin.

3.3.1 Alexa-488 labelled toxin highlights aggregation sites on the lipid membrane

The use of a fluorescently labelled α-toxin allows the toxin activity to be monitored in real-time using fluorescence microscopy. Due to the high rate of enzyme activity, a compromise has to be made between using a toxin concentration that is sufficiently high to produce detectable fluorescence but low enough to prevent the lipids immediately hydrolysing and rupturing the GUV. For our preparations the optimum was found to be ≈ 64 nM.

Figure 5 shows a typical DOPC vesicle imaged using confocal microscopy 20 minutes after alexa-488 labelled α-toxin was added to the vesicle suspension. The sucrose-solution filled vesicle appears as a dark circular shadow on a brighter background produced by the fluorescently labelled toxin dispersed in the host solution. Sub-micron sized aggregates of the labelled toxin are visible around the circumference of the vesicle. These fluorescent spots had around twice the intensity of the background fluorescence and were only seen at the membrane-solution interface. This suggests that the toxin tends to aggregate on the membrane during the initial stages of the interaction. After a further 20 minutes the contrast between the interior and exterior of the vesicle became less clear suggesting that the membrane became permeable to the fluorescently labelled enzyme (data not shown).

FIGURE 5

Figure 5. Confocal fluorescence images of Alexa-488 labelled α-toxin interacting with a DOPC giant unilamellar vesicle (arrows highlight regions of increased fluorescence).

3.3.2 Ratiometric imaging of Di-8-ANEPPS-labelled vesicles shows a non-uniform membrane dipole potential distribution after exposure to the toxin

Labelling GUVs with the electrochromic probe Di-8-ANEPPS allows the membrane dipole potential of lipid vesicles to be quantified. For a suitably low dye concentration, the dye molecules partition into the lipid bilayer, causing minimal disruption to the integrity of the GUV membrane. Imaging the Di-8-ANEPPS-labelled vesicles at two separate excitation wavelengths, 420 nm and 520 nm, and calculating the ratio of the fluorescence intensity collected in each case removes any inaccuracies arising from non-uniform dye distribution when calculating the value of ψ_d. The absolute value of the membrane dipole potential depends on the lipid head-group, molecular packing density, vesicle radius and the structure of water molecules in the headgroup region. In the absence of toxin, a spherical GUV with no visible defects (e.g. attachments, daughter vesicles etc.) formed from a single lipid species shows uniform fluorescence intensity across the surface and the potential is essentially constant.

Figure 6A shows a typical fluorescence microscopy image of a vesicle labelled with Di-8-ANEPPS after ten minutes incubation with α-toxin at a concentration of 64 nM. The intensity of the fluorescence around the edge of the vesicle is clearly non-uniform with enhanced fluorescence intensity in the lower left region of the two fluorescence images. Such bulges exhibiting heightened fluorescence intensity (and not present immediately after the addition of toxin) were found to develop over time in many vesicles after the addition of toxin (see below). This suggests higher local concentrations of Di-8-ANEPPS in this region. The absolute value for ψ_d (in mV) can be found using the expression:

$$\psi_d = \frac{R+0.3}{0.0043} \qquad \text{(Eq. 2)}$$

where R is the ratiometric intensity (given by $I_{420\text{ nm}}/I_{520\text{ nm}}$)[29]. Analysis of the ratiometric image (Figure 6A(iii)) suggests that the mean membrane dipole potential value in the majority of the membrane is 350 ± 30 mV but at the site of the droplet it is 400 ± 30 mV. In comparison, the membrane dipole potential measured for a similar sized, un-exposed vesicle is 375 mV ± 14 mV and there is no evidence of regional variations on the membrane. The small increase in membrane potential can be attributed to an increase in lipid packing at the site of the droplet. The value of ψ_d differs by 14 % between the two regions of the post-toxin vesicle. This is likely to arise from the change in surface morphology and increase in local curvature in the membrane[30] around the DAG droplet which enables a change in lipid packing as well as changes in spatial organisation of lipid molecules with respect to each other, lipid headgroup configuration and headgroup-associated water. Within the measurement accuracy, the difference, 50 ± 42 mV, appears small. However, this is not unexpected, since as we have previously shown in red cell ghosts[30], curvature effects are of the order of 30 mV.

FIGURE 6

Figure 6. (A) Fluorescence microscopy images of a Di-8-ANEPPS labelled DOPC vesicle after 10 min incubation with α-toxin at (i) 420 nm excitation, (ii) 520 nm excitation and (iii) the ratiometric result ($I_{420\text{nm}}/I_{520\text{nm}}$). The colour scale indicates the equivalent membrane dipole potential values calculated using Equation (2); (B) Confocal images of a Di-8-ANEPPS labelled DOPC giant unilamellar vesicle after incubation with unlabelled α-toxin for (i) 10 minutes and (ii) 20 minutes. Excitation wavelength 454 nm. Note that these are not ratiometric images and therefore the image intensity is not suggestive for the value of the dipole potential of the membrane.

To check whether these spatial inhomogeneities were a result of the lytic activity of the toxin, we performed time-lapse fluorescence confocal imaging. Ratiometric imaging was not possible with our confocal microscope, but the excitation wavelength of 454 nm provided high-resolution imaging of Di-8-ANEPPS labelled vesicles and a representative example is shown in Figure 6B. The confocal images were collected with the focal plane set midway through the vesicle at its widest point. During the first 10 minutes of incubation with the toxin (Figure 6B(i)) the vesicle has fairly uniform fluorescence around its circumference indicating that the dye is uniformly absorbed across the surface. Figure 6B(ii) shows a cross-section through the same vesicle a further 10 minutes later and the formation of bright "droplets" in the membrane can be clearly seen with a size of around 0.5 µm. This is most likely due to the Di-8-ANEPPS partitioning better into the DAG droplets.

The "droplet" observations are in agreement with similar studies by Riske and co-workers on the interaction of the phospholipase C (including α-toxin) with 1-stearoyl-2-oleoyl-sn-glycero-3-phosphocholine (SOPC) vesicles[31] which showed the formation of diacylglycerol (DAG) droplets in the lipid bilayer which were characterised by a number of techniques (fluorescence microscopy, differential scanning calorimetry, fluorescence anisotropy measurements, and small angle x-ray scattering). Furthermore, fluorescence images collected using NBD-DPPE in the SOPC membrane showed that the DAG droplets were highly fluorescent indicating a significant partitioning of the labelled phospholipid into the DAG-rich domains, consistent with the present observations.

Accumulation of hydrolysis products in droplets embedded in the membrane is not restricted to artificial lipid bilayers. At higher toxin concentrations, we observed droplet formation in RBC membranes as well (see Figure S1, Supplementary Information).

3.4 Exposure of red blood cells to α-toxin results in morphological change and focal accumulation of hydrolysis products.

The human red blood cell has a well-characterised lipid membrane, a membrane protein content of 23 % (by area)[32], a cytoskeleton and a rudimentary glycocalyx and is therefore ideal for examining the effects of their structural complexities on toxin interaction including the secondary processes that occur once the initial interaction of the toxin with the membrane has taken place.

3.4.1 Ratiometric imaging of Di-8-ANEPPS labelled red blood cells exposed to the toxin shows a non-uniform membrane dipole potential distribution

Previous studies[30] have demonstrated that human red blood cell membranes can be readily labelled with Di-8-ANEPPS. Ratiometric imaging of healthy discotic RBCs indicates that ψ_d is of the order of 250 mV, varying by around 30 mV along the surface of the cell. As ψ_d is closely related to the lipid packing and membrane composition, it is reasonable to expect that changes to the membrane structure due to hydrolysis of the constituent lipids may translate into changes in the local value of ψ_d. (It is also possible that subsequent events occurring in the cell, e.g. caused by the release of the DAG and ceramide after lipid hydrolysis, may also contribute to these changes, but it is not possible to distinguish between these events in the current study).

Figure 7 shows fluorescence microscopy images of a red blood cell labelled with Di-8-ANEPPS and imaged using an excitation wavelength of 420 nm and emission wavelength of 650 nm during incubation with 1.4 nM α-toxin (this image sequence is not suggestive for the value of the dipole potential as it does not show the ratio). At this concentration the initial change in the cell is very rapid and the cell had already become a non-axisymmetric stomatocyte within the first 2 minutes, as indicated by the elongation of the central dimple in the cell. The highly curved perimeter of this central indentation appears as a bright ring of fluorescence from the Di-8-ANEPPS dye in the membrane. Approximately 18 minutes after the addition of the toxin the fluorescent central ring of the red blood cell becomes increasingly fragmented forming distinct droplets. This effect is comparable to the localisation of the dye seen during measurements made on Di-8-ANEPPS labelled

DOPC vesicles, and is associated with the partitioning of the dye into the DAG-rich regions (as explained earlier, see also Figure S1, Supplementary Information).

FIGURE 7

Figure 7. Fluorescence microscopy images of a Di-8-ANEPPS labelled red blood cell (excitation at 420 nm) illustrating the change in dye distribution over time during incubation with 1.4 nM α-toxin.

Figure 8 shows ratiometric images indicating that in the regions of significant membrane-toxin interaction ψ_d decreases by around 50 ± 40 mV, equivalent to a change in electric field of 10^7 V m^{-1}, between the start and end of the incubation process. Unlike the images of absolute fluorescence intensity in Figure 7 showing bright droplets in the cell membrane towards the end of the experiment, the ratiometric images in Figure 8 do not show any significant localised changes in the membrane dipole potential in the same vicinity. Instead, ψ_d has locally decreased significantly 20 minutes after the addition of the toxin and then appears to recover a more uniform distribution towards the end of the incubation with the average value of ψ_d across the majority of the cell approximately 20 mV lower than at the beginning of the study.

FIGURE 8

Figure 8. Ratiometric fluorescence microscopy images showing the membrane dipole potential across a Di-8-ANEPPS labelled red blood cell during incubation with α-toxin. The colour scale indicates the corresponding value for the membrane dipole potential calculated using Equation (2).

The trend observed here, i.e. a decrease in the dipole potential, is opposite to the one for giant vesicles (Figure 6) where the dipole potential increased in the regions of high toxin activity. We hypothesise that this is due to the presence of a membrane skeleton in RBCs. The decrease in membrane potential at the centre of the red blood cell reflects the decrease in lipid packing density[15]. The hydrolysis of the lipids in the membrane and the removal of the lipid headgroups from the lipid bilayer will produce an overall decrease in lipid packing density and hence a reduction in the membrane dipole potential. The decrease in packing is also in agreement with the observed decrease in surface pressure observed during the initial monolayer measurements made using the Langmuir trough (Figures 3 and 4) which arises due to the removal of substrate lipids from the monolayer by the hydrolysis process. The presence of the cytoskeleton in the cell hinders the ability of the cell membrane to significantly contract to accommodate this loss resulting in a decrease of the membrane dipole potential. In contrast, the vesicles were able to adapt to the change in lipids present in the membrane, producing an increase in membrane potential due to the lipids packing accordingly around the DAG droplets.

3.4.2 Exposure of red blood cells to α-toxin disrupts the cell morphology

The human red blood cell contains a high concentration of haemoglobin, uniformly distributed through the cytoplasm. Haemoglobin has a strong absorption band at a wavelength of 415 nm and analysis of the absorption of 415 nm light allows the cell morphology to be determined[33]. To a first approximation, the optical density (absorbance) varies linearly with the thickness of haemoglobin present in the beam path and hence a healthy RBC in the form of a biconcave disc appears as a dark annulus with a brighter centre. Monitoring the change in absorbance across the cell as it is exposed to toxin allows changes in cell shape to be evaluated.

Snapshots of a red blood cell incubated in 1.4 nM α-toxin using 415 nm light for different times are shown in Figure 9. Initially the cell has a biconcave disc shape. As the incubation progresses, 12 minutes after the addition of the toxin the image indicates a stomatocytic cell which has a cup-like shape with the haemoglobin distributed around the perimeter. After this point invaginations appear around the central region and the diameter of the cell begins to decrease as the cell folds inwards resulting in a “crinkled” effect on the surface. This shape sequence suggests a decrease in the membrane differential area (i.e. the difference in area between the outer and the inner leaflets) due to hydrolysis, which shifts the cell from the original discocyte first to an axisymmetric stomatocyte and then to a non-axisymmetric stomatocyte[34]. Finally the cell shrivels to a slightly oblate shape. This response was common to all of the cells in the field of view with the onset of the initial disruption for individual cells occurring over a 10 minute period for this toxin concentration, but with comparable rate of morphological changes.

FIGURE 9

Figure 9. Microscopy images illustrating the change in transmission of 415 nm light through a red blood cell during incubation with α-toxin. Low intensity corresponds to high absorption.

Figure 10A shows the radially averaged absorption as a function of the distance from the centre of the cell at selected times after the addition of the α-toxin. The averages were obtained from the images in Figure 9 (after calculating the optical density) by using an ImageJ radial averaging plug-in. The radial absorbance produced is only an approximation as the calculation assumes that the cell has radial symmetry which, as can be seen in Figure 9, is not true between 12 and 20 minutes after the addition of the toxin when the symmetry is broken. Despite this deviation the results can be used to illustrate changes in morphology and local cell thickness. Figure 10B (circles) shows the calculated mean cell radius as a function of time. The graph suggests that, after a short delay of about 8 min, the cell radius decreases at a steady rate during the incubation procedure. In the next section, the cell morphological response to toxin in the initial stages of interaction is considered in more detail.

Analysis of the integrated optical density of the red blood cell in each image allows the change in haemoglobin content of the cell to be monitored (Figure 10B, squares). We were able to quantify the total quantity of haemoglobin between t = 10 min and t = 22 min and the calculations show that during this time period, the integrated absorbance has steadily reduced by about 6%. This suggests that part of the cytoplasmic haemoglobin has leaked out of the cell as a result of the enzymatic activity of the toxin. However, as can be seen from Figure 9, the process of haemolysis is not full even after 30 min toxin exposure (after this point, very little change is observed in the cell). This is consistent with observations that, when exposed to α-toxin, the amount of haemolysis is limited even when the toxin concentration is subsequently increased[35]. The mechanism by which the haemoglobin is released is currently unclear. Studies on the interaction of α-toxin with mammalian erythrocytes suggest that lysis is not solely due to the loss of the membrane integrity due to the hydrolysis of substrate lipids[36]. Measurements on the interaction of the toxin with horse erythrocytes (which have a different membrane lipid composition) suggest that the interaction of the toxin with receptors on the erythrocyte membrane also play an important role, such as through the uptake of Ca^{2+} through T-type Ca^{2+} channels indirectly activated by the toxin[37]. In addition, the red blood cell inner and outer leaflet lipid mixture monolayer studies reported in section 3.1 suggest that the inner leaflet of the red cell may be less susceptible to interactions with the toxin than the outer leaflet which may add a degree of protection against lysis.

Our experiments show that red cells respond to α-toxin in a concentration-dependent manner: at low concentrations, the toxin is able to elicit morphological changes but not necessarily lyse the cell; at higher concentrations, morphological changes are accompanied by (partial) loss of haemoglobin by the cell. Figures S2-S4 (Supplementary Information) show a typical cell response to low toxin concentration. Here, the toxin is able to significantly change the morphology of the cell (Figures S2 and S3), but the total concentration of haemoglobin in the cell as measured using the optical density, remains constant (Figure S4). This behaviour is different from the cell response to higher toxin concentrations (Figure 10) where the morphological changes are accompanied by loss of haemoglobin by the cell. Figure S5 (Supplementary information) shows the response of a red blood cell exposed to a different type of toxin (a pore-forming toxin), where the onset of lysis can be clearly identified from the sudden drop in the integrated optical density.

FIGURE 10

Figure 10. (A) Variations of the absorbance of 415 nm light with radius indicating the relative change in cell thickness (the images are included for illustrative purposes and correspond to these in Figure 9); (B) Change of the mean cell radius (circles, left axis) and integrated optical density (squares, right axis) with time.

3.4.3 Thermal fluctuation spectroscopy reveals a two-stage interaction between α-toxin and RBC.

Using phase-contrast microscopy, it is possible to continuously monitor the evolution of the RBC shape in response to the interaction with α-toxin. As described in Section 2.5.4, the cell response to α-toxin was monitored by recording 40 s video sequences first at $t = 0$ (before the addition of toxin) and then periodically after exchanging the solution. A small concentration of toxin (0.18 nM) was deliberately used in an attempt to monitor the initial stages of interaction between the toxin and the cell membrane. Figure 11 shows a typical example of the changes in the equatorial contour radius R (i.e. the zeroth Fourier amplitude, see Equation (1) and Figure 2) of two cells as a function of time. At this toxin concentration, two distinct regimes are observed. Initially, R remains constant and close to the radius of the untreated cell. After this initial period, a rapid decrease in the radius is observed, which is evidence for loss of membrane area and/or change in the 3D shape of the RBC. Experiments suggest that the initial regime (i.e. constant R) may have different duration for each cell, as also evident from Figure 11, where the onset of radius change differs for the two cells by some 13 min (see the vertical dashed lines). This by itself is an interesting observation, and may be due to differences in the local toxin concentrations in the observation chamber though every effort was made to ensure thorough mixing. Another more likely possibility is that different cells may have different susceptibilities to the toxin, depending on the physical and biochemical properties of their membranes, which could be modified due to their age, exposure to oxidative and other types of chemical stress etc. This observation correlates well with the fact that lysis occurs over time and is not synchronous.

FIGURE 11

Figure 11. Time dependence for the normalised (with respect to t = 0) contour radius for two cells. The initial time t = 0 corresponds to cells unexposed to toxin. After that, a toxin-containing buffer is introduced and the contour radius adjusts as a result of the cell interaction with the toxin. The vertical dashed lines (at t = 1020 s and t = 1800 s) show the onset of the radius decrease.

Analysis of the rest of the Fourier modes reveals more information about the subtle changes in shape the cells go through as a result of the incorporation of the toxin in the membrane. A comprehensive description of the mechanism behind the stomatocyte-discocyte-echinocyte shape sequence of the red cell can be found in[34] based on minimisation of the full elastic energy of the cell membrane, including contributions from the lipid bilayer and the membrane skeleton. The model predicts that, upon increasing the effective area difference between the two leaflets of the erythrocyte membrane, a discocytic red cell will undergo a *continuous* transition to a flat echinocyte with 9 bulges around the equator (the so-called E1-9 shape)[34]. For the shape representation we use, Equation (1), this would imply increasing the Fourier amplitude of the 9th mode. Figure 12A is an illustration for such a shape change of a 2D contour: the initial circular shape (which, in the ideal symmetrical case would be the 2D equatorial section of a discocyte) is transformed into a contour possessing nine bulges. The example in Figure 12A is exaggerated to make the shape change clearly visible; in the results described below, the shifts we observe are significant but much smaller, which makes it impossible for the shape changes to be noticed by simple visual inspection of the phase contrast images. Nevertheless, the Fourier analysis of the modes reveals reproducible changes in the cell morphology.

FIGURE 12

Figure 12. (A) Example of changes in the 2D equatorial contour shape (see Equation (1)). Increasing the value of the ninth Fourier amplitude whilst keeping R constant results in an echinocytic shape. (B, C) Time dependences of the normalised contour radius (solid circles, left axis) and mode 9 amplitude (green dots, right axis) in the vicinity of the transition to hydrolysis. The mean values of c_9 are represented by short horizontal black lines. The short vertical lines indicate the onset of the second stage of interaction. The lines connecting the data points are guides to the eye only.

Initial incorporation of toxin in the outer membrane leaflet of a discocytic cell will lead to small increases in the membrane differential area, therefore we can expect to see a shift towards an echinocyte. In the ideal case (i.e. the discocyte-echinocute transition occurs under quasi-equilibrium conditions) one may expect changes only in the 9th mode, since the echinocytic shape emerging from this transition has 9 bulges around the periphery, as predicted by the theory[34]. In reality, the membrane is constantly fluctuating whilst undergoing transition, adapting its shape in response to the toxin, and this situation is clearly not quasi-equilibrium. One could therefore expect general increases in the higher modes (e.g. 5-10), a fingerprint for the propensity of the cell to form bulges as it transitions to an echinocyte. Once the toxin begins its enzymatic cleavage of the outer leaflet, the shape relaxes back to discocytic and the amplitudes of these modes decrease. We monitored the behaviour of the higher modes (5th-10th) of six cells, and their amplitudes exhibited maximums around the onset of radius decrease. To illustrate this behaviour, Figure 12B,C shows trends in the ninth mode, for the same two cells as in Figure 11, in the vicinity of the onset of change in radius (1020 s and 1080 s, respectively, see the vertical dashed lines). The solid circles show the change in R immediately before and after the onset of the second regime. Beneath them the evolution of c_9 is plotted. Due to the membrane thermal flicker, one observes sizeable fluctuations in this mode (represented by the clusters of green dots), superimposed on the trends in the mean value $\langle c_9 \rangle$ of this mode's amplitude (represented as horizontal solid lines through each green cluster). It is clear from the figure that, immediately before the threshold (shown by the small vertical dashed lines), $\langle c_9 \rangle$ shows a small increase, which is an evidence for a transition to a slightly echinocytic shape (see Figure 12A). This most probably is due to the first stage of the toxin interaction with the bilayer lipid membrane, i.e. the penetration and incorporation of the C-domain into the outer leaflet of the RBC membrane. This will result in an increase in the area of the outer monolayer compared to the inner one, which will drive the cell towards a more convex shape, that is the echinocytic shape in the main stomatocyte-discocyte-echinocyte RBC shape sequence[34, 38, 39]. Once the toxin begins its hydrolysing activity, we observe a concurrent decrease in the contour radius R and $\langle c_9 \rangle$ (see Figure 12B,C to the right of the vertical dashed lines). Cleavage of lipid now results in loss of area of the outer monolayer, which drives the shape in the opposite direction through a discocyte towards a stomatocyte. This transition is reflected in the 2D equatorial contours as circular cross-sections with gradually decreasing R and $\langle c_9 \rangle$. Such a transition towards stomatocytic shapes is clearly visible in Figure 9 (with the later stages also observable in Figure 7).

The effects reported here on contour shapes and hence the changes in $\langle c_9 \rangle$ are small. Further justification for this methodology is offered in the Supplementary Information, where we present two model experiments (Figures S6 and S7), in which we deliberately induced transitions between discocytic and echinocytic shapes, and monitored the response of c_9. The results clearly demonstrate the potential of this method to identify quantitatively morphological changes.

The two stages of interaction identified here correspond well to the mechanism of interaction between α-toxin and lipid membranes proposed previously: an initial incorporation of the C-domain into the outer layer of the membrane with subsequent hydrolysing action by the active N-domain[40]. The small but reproducible increase in the magnitude of the higher Fourier mode amplitudes most likely corresponds to the incorporation of the toxin into the outer membrane leaflet, which results in subtle changes of cell morphology. In the second, hydrolysing, stage of toxin activity the membrane differential area decreases and as a consequence the cell undergoes a transition towards more concave, stomatocytic shapes, and this process is characterised with a decrease in the apparent contour radius and the magnitudes of the higher Fourier modes. Similar trends have been observed also during the interaction between Phospholipase C and giant lipid vesicles[31, 41]. These results suggest that soft lipid membranes, through Fourier-based shape and thermal fluctuation analysis, can be used as sensitive probes to monitor interactions with bacterial toxins.

Conclusion

The interaction of α-toxin with lipid monolayers and bilayers produces profound changes in the biophysical properties of the membrane. Measurements of the initial toxin-lipid interaction using monolayers from substrate lipids show a significant decrease in surface pressure after lipid hydrolysis. For non-substrate lipids, the toxin still inserts into the membrane at physiological packing densities but does not show any lipase activity. Studies of the toxin interacting with lipid bilayers, in the form of vesicles indicate that the DAG products produced from the lipid hydrolysis are deposited in localised regions within the membrane causing localised swellings in the lipid bilayer. This is accompanied with a local increase in the dipole potential, most probably due to the induced curvature. Measurements made on the red blood cell suggest that, in contrast to the observations made in the case of lipid vesicles, the membrane dipole potential decreases after incubation with the enzyme. This suggests that the presence of the cytoskeleton (and possibly secondary processes which follow the initial membrane-toxin interaction) prevent the membrane from shrinking to accommodate the decrease in lipid area. Red cells exposed to α-toxin undergo reproducible and well-defined morphological transitions. The analysis of the mean cell shapes during their interactions with α-toxin reveals clearly identifiable stages of toxin incorporation followed by lipid hydrolysis.

Acknowledgements

This work was funded through a Royal Society University Research Fellowship held by SAJ. The authors would like to thank Miss C. Muttram for assistance with the Langmuir trough data collection. We thank Dr J. Sleep and Dr D. Woods for many helpful discussions.

REFERENCES

1. E. L. Wu, X. Cheng, S. Jo, H. Rui, K. C. Song, E. M. Dávila-Contreras, Y. Qi, J. Lee, V. Monje-Galvan and R. M. Venable, *J. Comp. Chem.*, 2014, **35**, 1997.
2. The PyMOL Molecular Graphics System, Version 1.7.4, Schrödinger, LLC.
3. R. V. Titball, C. E. Naylor and A. K. Basak, *Anaerobe*, 1999, **5**, 51.
4. C. E. Naylor, J. T. Eaton, A. Howells, N. Justin, D. S. Moss, R. W. Titball and A. K. Basak, *Nat. Struct. Mol. Biol.*, 1998, **5**, 738.
5. J. H. Exton, *J. Biol. Chem.*, 1990, **265**, 1.
6. S. L. Pelech and D. E. Vance, *Trends Biochem. Sci.*, 1989, **14**, 28.
7. M. Nagahama, K. Michiue and J. Sakurai, *BBA-Biomembranes*, 1996, **1280**, 120.
8. M. Nagahama, K. Michiue, K. Kobayashi and J. Sakurai, *Jpn. J. Med. Sci. Biol.*, 1996, **49**, 249.
9. P. Urbina, M. Flores-Diaz, A. Alape-Girón, A. Alonso and F. M. Goñi, *BBA-Biomembranes*, 2011, **1808**, 279.
10. G. Basáñez, J. L. Nieva, F. M. Goñi and A. Alonso, *Biochemistry*, 1996, **35**, 15183.
11. F. M. Goñi, L.-R. Montes and A. Alonso, *Prog. Lipid Res.*, 2012, **51**, 238.
12. M. Ibarguren, D. J. López, L.-R. Montes, J. Sot, A. I. Vasil, M. L. Vasil, F. M. Goñi and A. Alonso, *J. Lipid Res.*, 2011, **52**, 635.
13. M. Ibarguren, J. Sota, L.-R. Montesa, A. I. Vasil, M. L. Vasil, F. M. Goñi and A. Alonso, *Chem. Phys. Lipids*, 2013, **166**, 12.
14. L. Chao, A. P. Gast, T. A. Hatton and K. F. Jensen, *Langmuir*, 2011, **26**, 344.
15. R. J. Clarke, *BBA-Biomembranes*, 1997, **1327**, 269.
16. P. O'Shea, *Biochem. Soc. Trans.*, 2003, **31**, 990.
17. P. O'Shea, *Phil. Trans. R. Soc. A*, 2005, **363**, 575.
18. V. Montana, D. L. Farkas and L. M. Loew, *Biochemistry*, 1989, **28**, 4536.
19. D. L. Stevens, J. Mitten and C. Henry, *J. Infect. Dis.*, 1987, **156**, 324.
20. M. I. Angelova and D. S. Dimitrov, *Faraday Discuss.*, 1986, **81**, 303.
21. W. S. Rasband, ImageJ, U. S. National Institutes of Health, Bethesda, Maryland, USA, http://imagej.nih.gov/ij/, 1997-2014.
22. J. P. Hale, G. Marcelli, K. H. Parker, C. P. Winlove and P. G. Petrov, *Soft Matter*, 2009, **5**, 3603.
23. J. P. Hale, C. P. Winlove and P. G. Petrov, *Biophys. J.*, 2011, **101**, 1921.
24. H.-G. Döbereiner, G. Gompper, C. K. Haluska, D. M. Kroll, P. G. Petrov and K. A. Riske, *Phys. Rev. Lett.*, 2003, **91**, 048301.
25. J. Pecreaux, H.-G. Döbereiner, J. Prost, J. F. Joanny and P. Bassereau, *Eur. Phys. J. E*, 2004, **13**, 277.
26. P. A. Janmey and P. K. J. Kinnunen, *Trends Cell Biol.*, 2006, **16**, 538.
27. C. Alonso, T. Alig, J. Yoon, F. Bringezu, H. Warriner and J. A. Zasadzinski, *Biophys. J.*, 2004, **87**, 4188.
28. P. G. Petrov, J. M. Thompson, I. B. A. Rahman, R. E. Ellis, E. M. Green, F. Miano and C. P. Winlove, *Exp. Eye Res.*, 2007, **84**, 1140.
29. T. Starke-Peterkovic, N. Turner, M. F. Vitha, M. P. Waller, D. E. Hibbs and R. J. Clarke, *Biophys. J.*, 2006, **90**, 4060.
30. S. A. Jewell, P. G. Petrov and C. P. Winlove, *BBA-Biomembranes*, 2013, **1828**, 1250.
31. K. A. Riske and H.-G. Döbereiner, *Biophys. J.*, 2003, **85**, 2351.
32. A. D. Dupuy and D. M. Engelman, *Proc. Natl. Acad. Sci.*, 2008, **105**, 2848.
33. J. Evans, W. Gratzer, N. Mohandas, K. Parker and J. Sleep, *Biophys. J.*, 2008, **94**, 4134.
34. G. Lim H. W., M. Wortis and R. Mukhopadhyay, in *Soft Matter, Vol. 4: Lipid Bilayers and Red Blood Cells*, eds. G. Gompper and M. Schick, WILEY-VCH Verlag GmbH & Co. KGaA, Weinheim, 2008, vol. 4, pp. 83-249.
35. J. Lenard and S. J. Singer, *Science*, 1968, **159**, 738.
36. J. Sakurai, S. Ochi and H. Tanaka, *Infect. Immun.*, 1993, **61**, 3711.

37. S. Ochi, M. Oda, M. Nagahama and J. Sakurai, *BBA-Biomembranes*, 2003, **1613**, 79.
38. G. Lim H. W., M. Wortis and R. Mukhopadhyay, *Proc. Natl. Acad. Sci.*, 2002, **99**, 16766.
39. M. P. Sheetz and S. J. Singer, *Proc. Natl. Acad. Sci.*, 1974, **71**, 4457.
40. J. Sakurai, M. Nagahama and M. Oda, *J. Biochem.*, 2004, **136**, 569.
41. H.-G. Döbereiner, P. G. Petrov and K. A. Riske, *J. Phys.-Condens. Mat.* , 2003, **15**, S303.

Figure Captions

Figure 1. α-toxin drawn as cartoon and coloured by the distance from the plane containing bound zinc and calcium ions (red into membrane, blue away from it). Exposed hydrophobic chains postulated to intercalate with hydrocarbon chains (F334, W214 and W217) are shown as sticks. The three zinc ions required for activity are shown in dark blue and the C-terminal calcium ions associated with the membrane binding are shown in lighter blue. 1,2-hexyl-phosphatidylcholine shown as spheres is modelled into the α-toxin active site by homology with its complex with *Bacillus cereus* PLC (PDBID 1P6D). The lipid bilayer (1-palmitoyl-2-oleoylphosphatidylcholine:cholesterol in 9:1 ratio) was generated using CHARMM-GUI[1] and is drawn as a semi-transparent surface. Figure drawn with PyMol[2].

Figure 2. Snapshot of a RBC in phase contrast (radius ~4 μm). The thin white line is the automatically traced equatorial contour.

Figure 3. Variation of surface pressure with time for lipid monolayers held at a constant area during a 1 hour exposure to α-toxin for (A) DOPC and DPPC, and (B) different lipid species.

Figure 4. Pressure versus area isotherms for lipid monolayers before (blue dotted line) and one hour after (red solid line) the introduction of α-toxin into the aqueous subphase. The lipids used are (A) DPPC; (B) DOPC; (C) PS (18:0)/PS (18:1) and (D) SM. In all cases the trough area is in arbitrary units.

Figure 5. Confocal fluorescence images of Alexa-488 labelled α-toxin interacting with a DOPC giant unilamellar vesicle (arrows highlight regions of increased fluorescence).

Figure 6. (A) Fluorescence microscopy images of a Di-8-ANEPPS labelled DOPC vesicle after 10 min incubation with α-toxin at (i) 420 nm excitation, (ii) 520 nm excitation and (iii) the ratiometric result (I_{420nm}/I_{520nm}). The colour scale indicates the equivalent membrane dipole potential values calculated using Equation (2); (B) Confocal images of a Di-8-ANEPPS labelled DOPC giant unilamellar vesicle after incubation with unlabelled α-toxin for (i) 10 minutes and (ii) 20 minutes. Excitation wavelength 454 nm. Note that these are not ratiometric images and therefore the image intensity is not suggestive for the value of the dipole potential of the membrane.

Figure 7. Fluorescence microscopy images of a Di-8-ANEPPS labelled red blood cell (excitation at 420 nm) illustrating the change in dye distribution over time during incubation with 1.4 nM α-toxin.

Figure 8. Ratiometric fluorescence microscopy images showing the membrane dipole potential across a Di-8-ANEPPS labelled red blood cell during incubation with α-toxin. The colour scale indicates the corresponding value for the membrane dipole potential calculated using Equation (2).

Figure 9. Microscopy images illustrating the change in transmission of 415 nm light through a red blood cell during incubation with α-toxin. Low intensity corresponds to high absorption.

Figure 10. (A) Variations of the absorbance of 415 nm light with radius indicating the relative change in cell thickness (the images are included for illustrative purposes and correspond to these in Figure 9); (B) Change of the mean cell radius (circles, left axis) and integrated optical density (squares, right axis) with time.

Figure 11. Time dependence for the normalised (with respect to $t = 0$) contour radius for two cells. The initial time $t = 0$ corresponds to cells unexposed to toxin. After that, a toxin-containing buffer is introduced and the contour radius adjusts as a result of the cell interaction with the toxin. The vertical dashed lines (at $t = 1020$ s and $t = 1800$ s) show the onset of the radius decrease.

Figure 12. (A) Example of changes in the 2D equatorial contour shape (see Equation (1)). Increasing the value of the ninth Fourier amplitude whilst keeping R constant results in an echinocytic shape. (B, C) Time dependences of the normalised contour radius (solid circles, left axis) and mode 9 amplitude (green dots, right axis) in the vicinity of the transition to hydrolysis. The mean values of c_9 are represented by short horizontal black lines. The short vertical lines indicate the onset of the second stage of interaction. The lines connecting the data points are guides to the eye only.

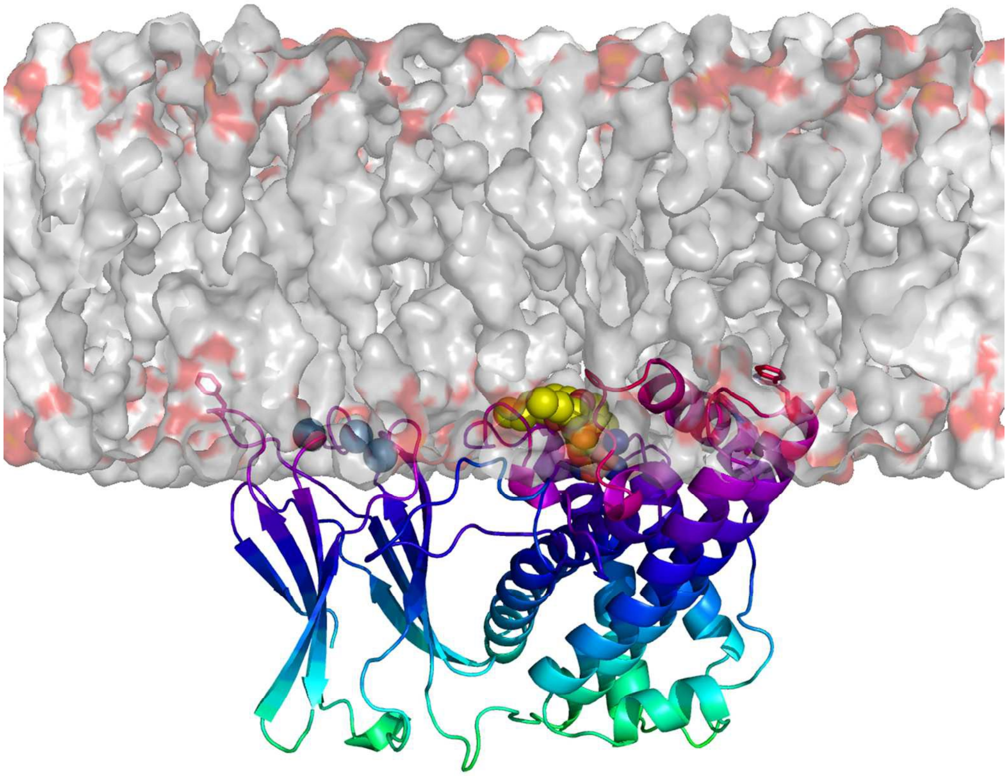

452x369mm (72 x 72 DPI)

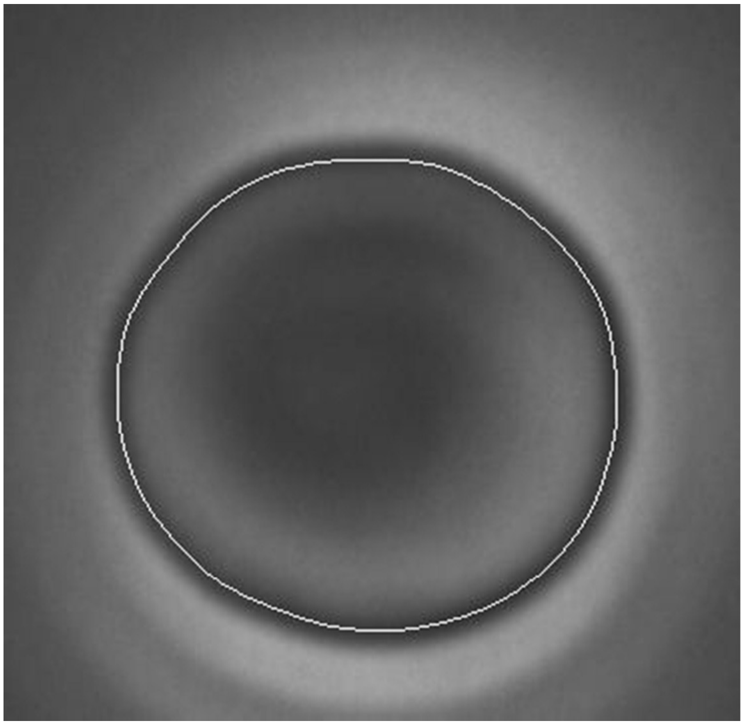

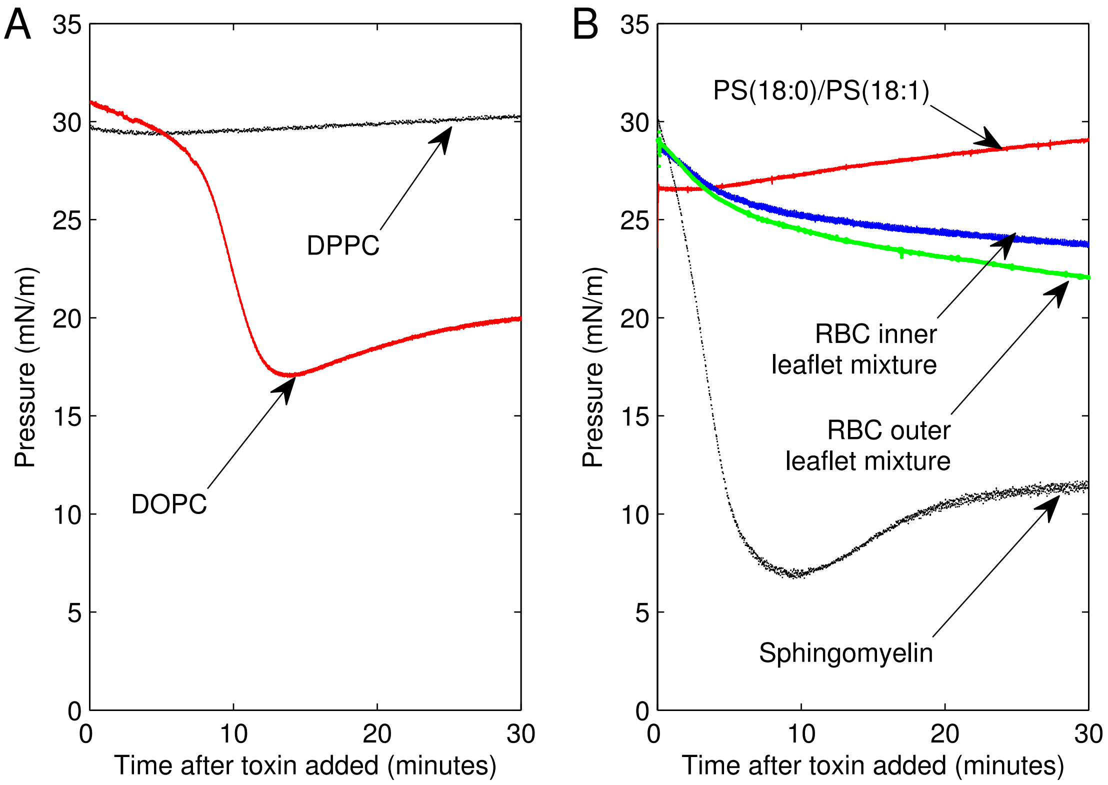
A
B
35
30
25
20
15
10
5
0
Pressure (mN/m)
Time after toxin added (minutes)
0
10
20
30
DPPC
DOPC
PS(18:0)/PS(18:1)
RBC inner
leaflet mixture
RBC outer
leaflet mixture
Sphingomyelin

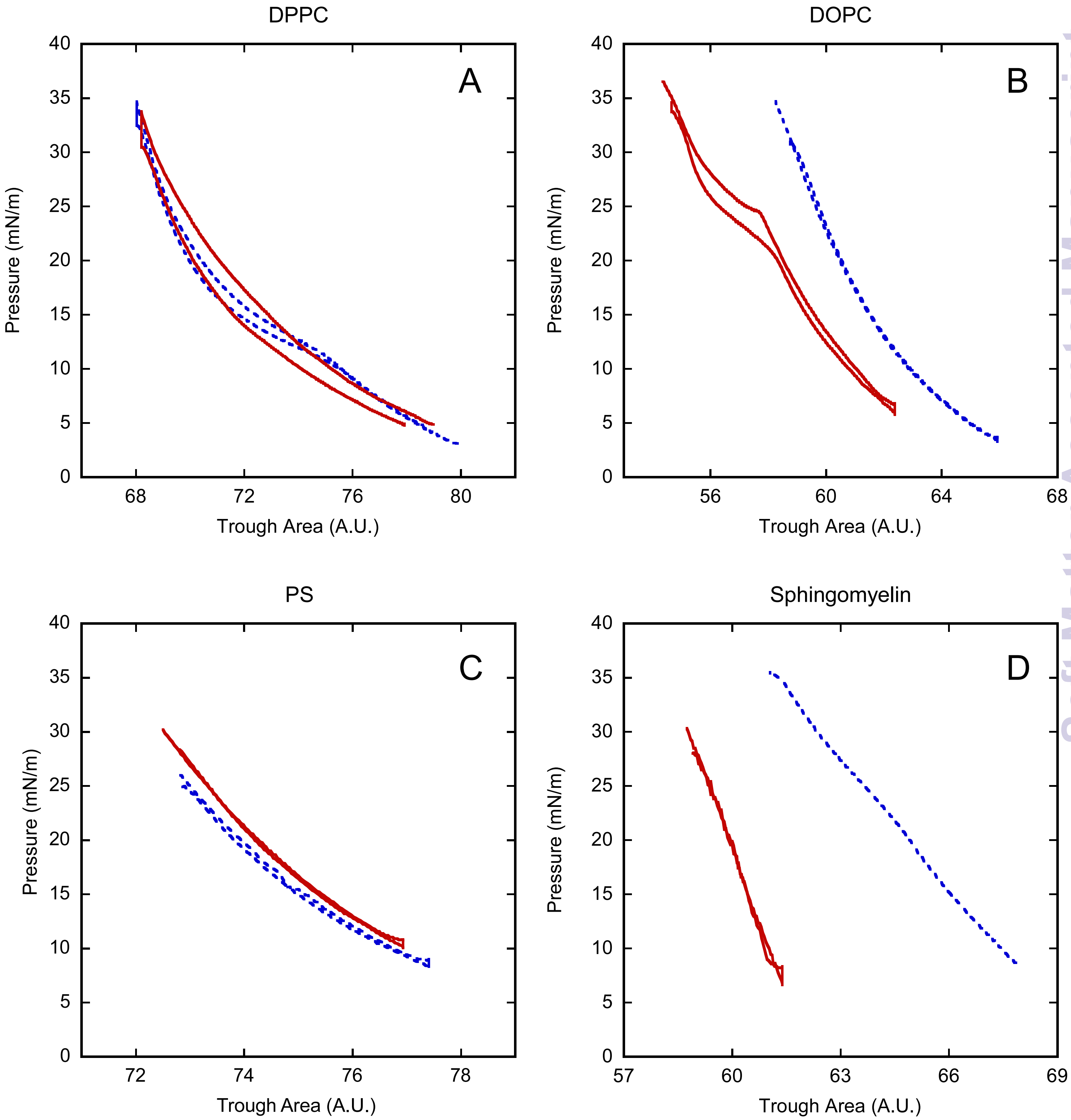
DPPC
A
DOPC
B
PS
C
Sphingomyelin
D
Pressure (mN/m)
Trough Area (A.U.)
0
5
10
15
20
25
30
35
40
68
72
76
80
56
60
64
68
72
74
76
78
57
60
63
66
69

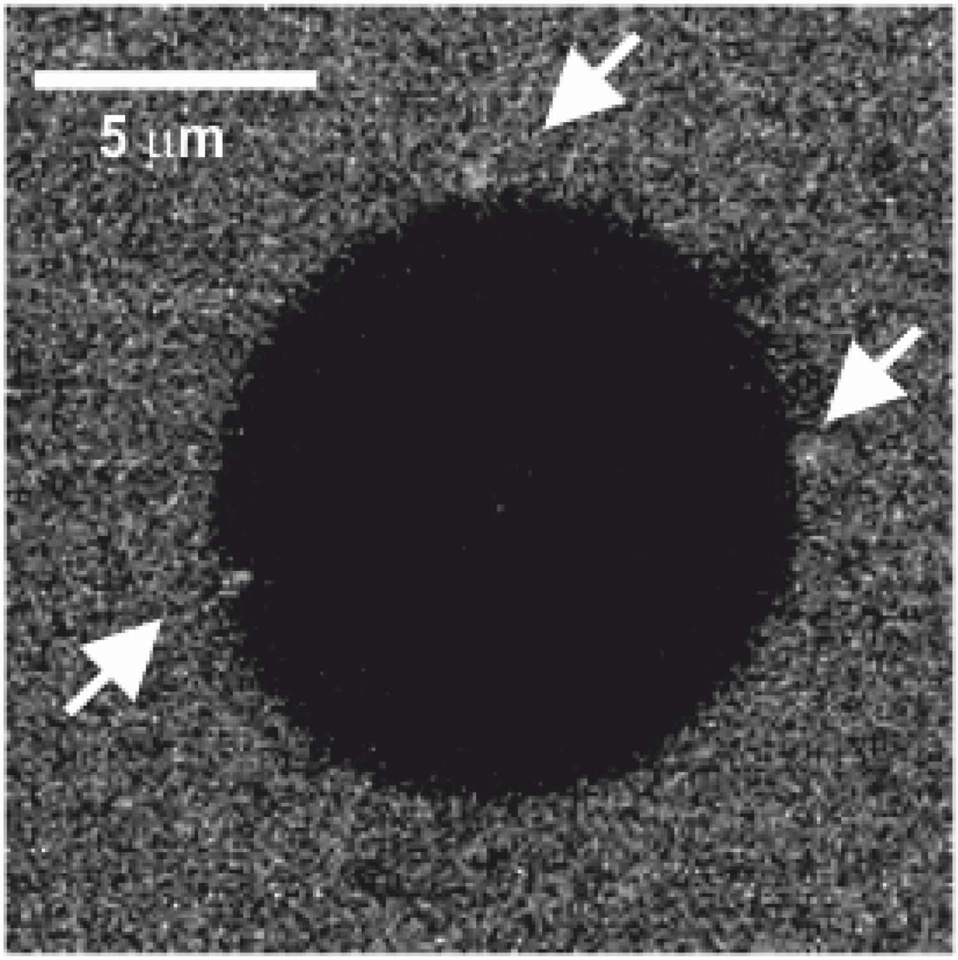
5 µm

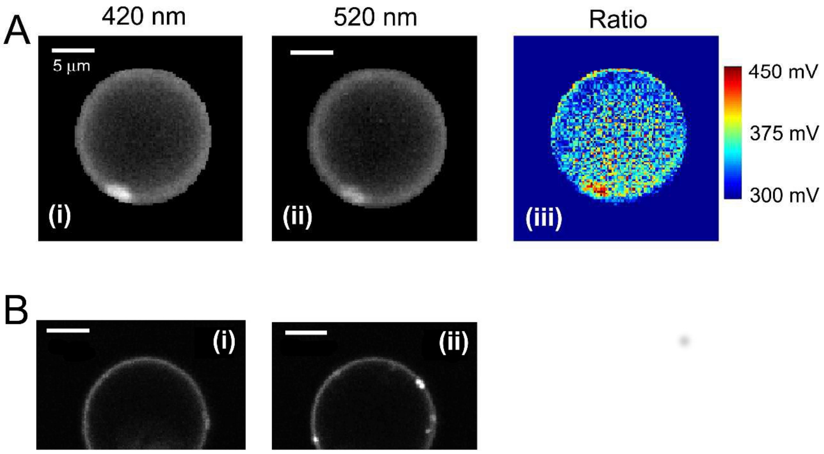
A
420 nm
520 nm
Ratio
5 μm
(i)
(ii)
(iii)
450 mV
375 mV
300 mV
B
(i)
(ii)

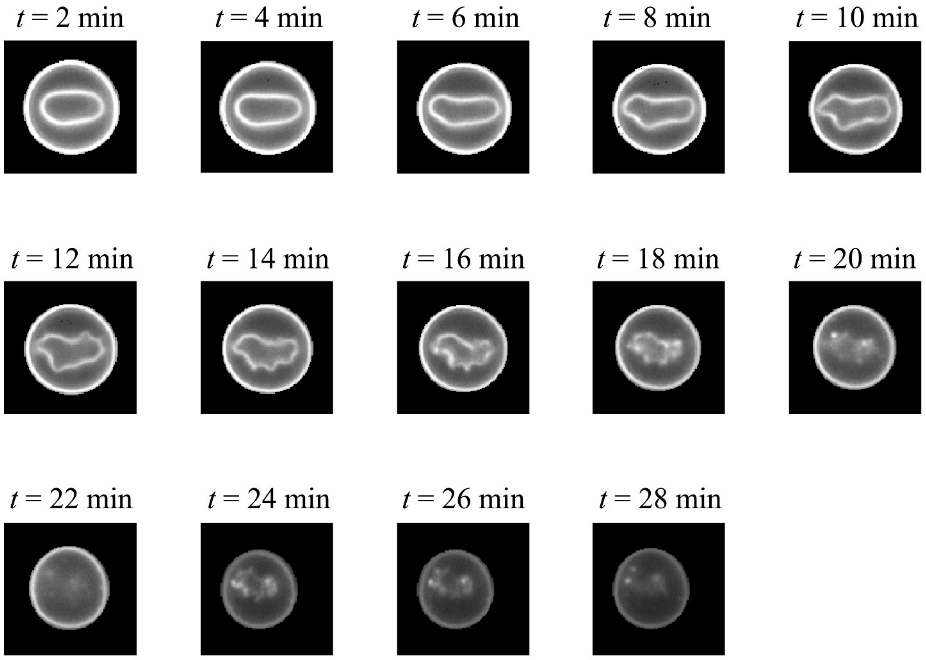
t = 2 min
t = 4 min
t = 6 min
t = 8 min
t = 10 min
t = 12 min
t = 14 min
t = 16 min
t = 18 min
t = 20 min
t = 22 min
t = 24 min
t = 26 min
t = 28 min

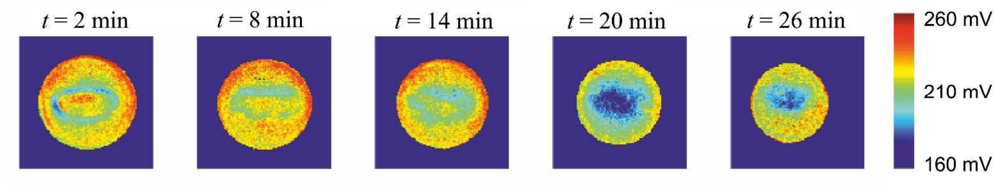
t = 2 min
t = 8 min
t = 14 min
t = 20 min
t = 26 min
260 mV
210 mV
160 mV

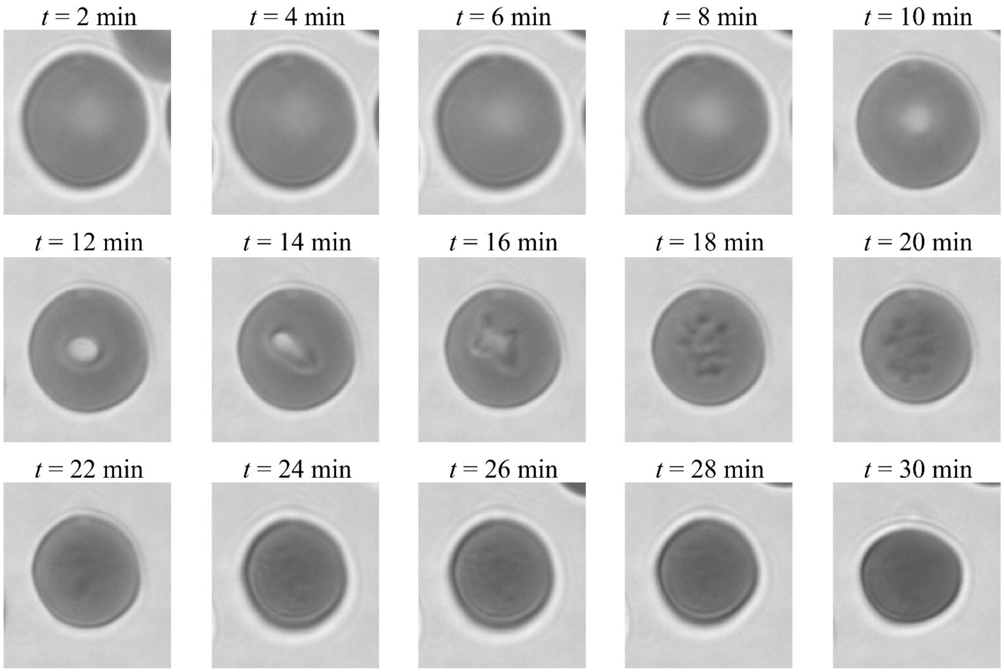
t = 2 min
t = 4 min
t = 6 min
t = 8 min
t = 10 min
t = 12 min
t = 14 min
t = 16 min
t = 18 min
t = 20 min
t = 22 min
t = 24 min
t = 26 min
t = 28 min
t = 30 min

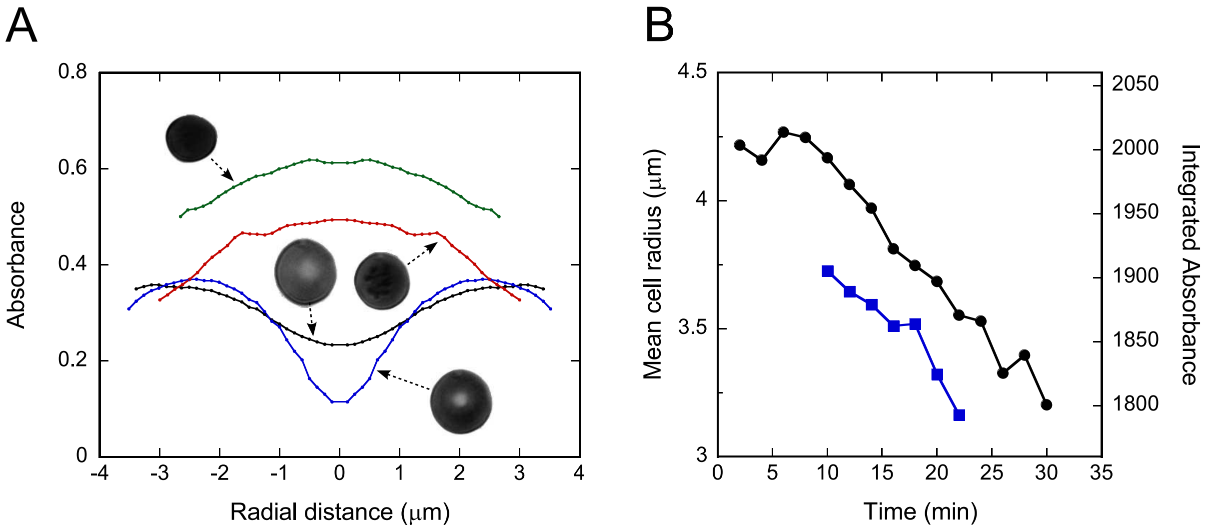
A
0.8
0.6
0.4
0.2
0
Absorbance
-4
-3
-2
-1
0
1
2
3
4
Radial distance (μm)
B
4.5
4
3.5
3
Mean cell radius (μm)
0
5
10
15
20
25
30
35
Time (min)
2050
2000
1950
1900
1850
1800
Integrated Absorbance

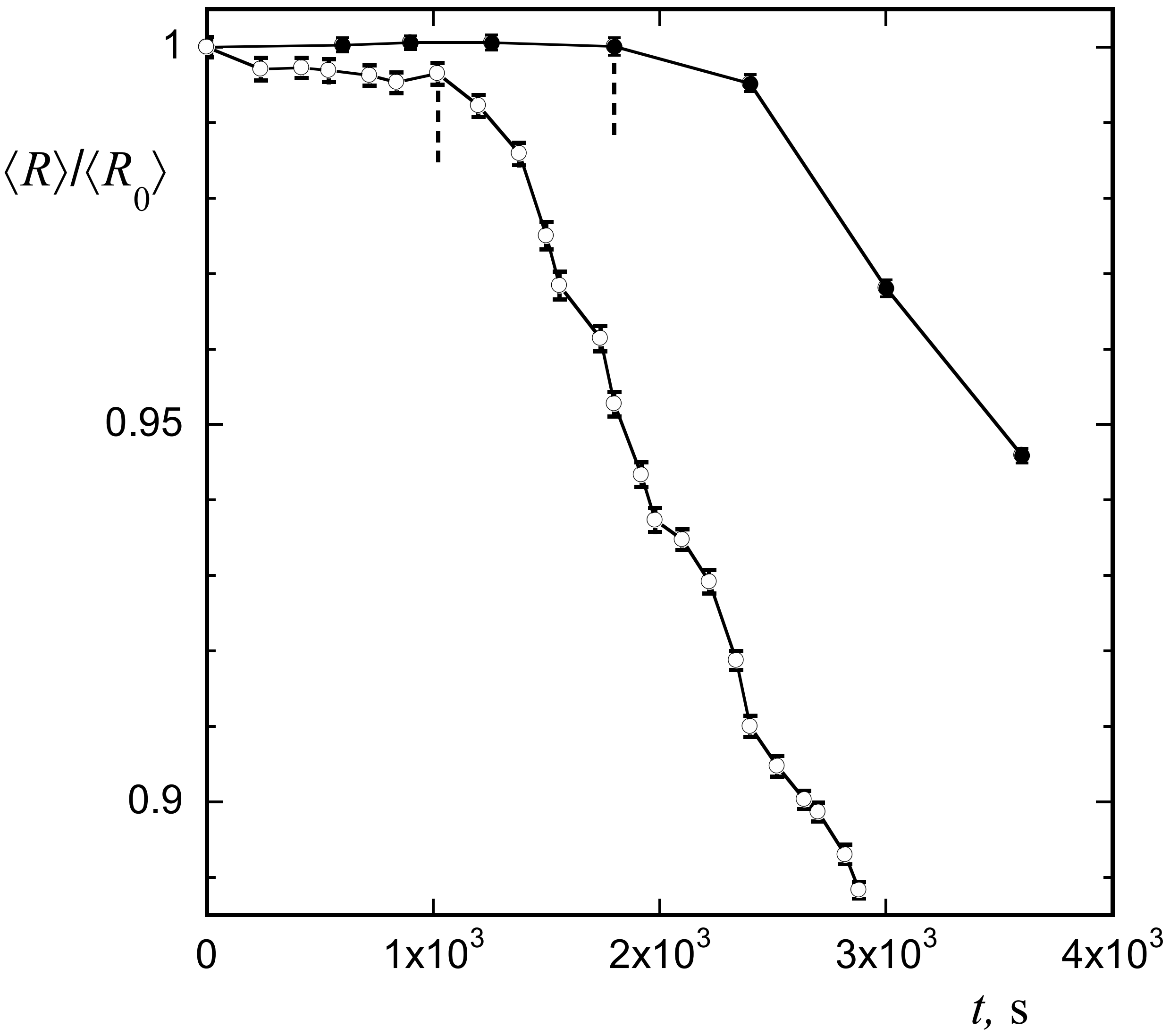
1
0.95
0.9
$\langle R\rangle/\langle R_0\rangle$
0
1x10^3
2x10^3
3x10^3
4x10^3
t, s

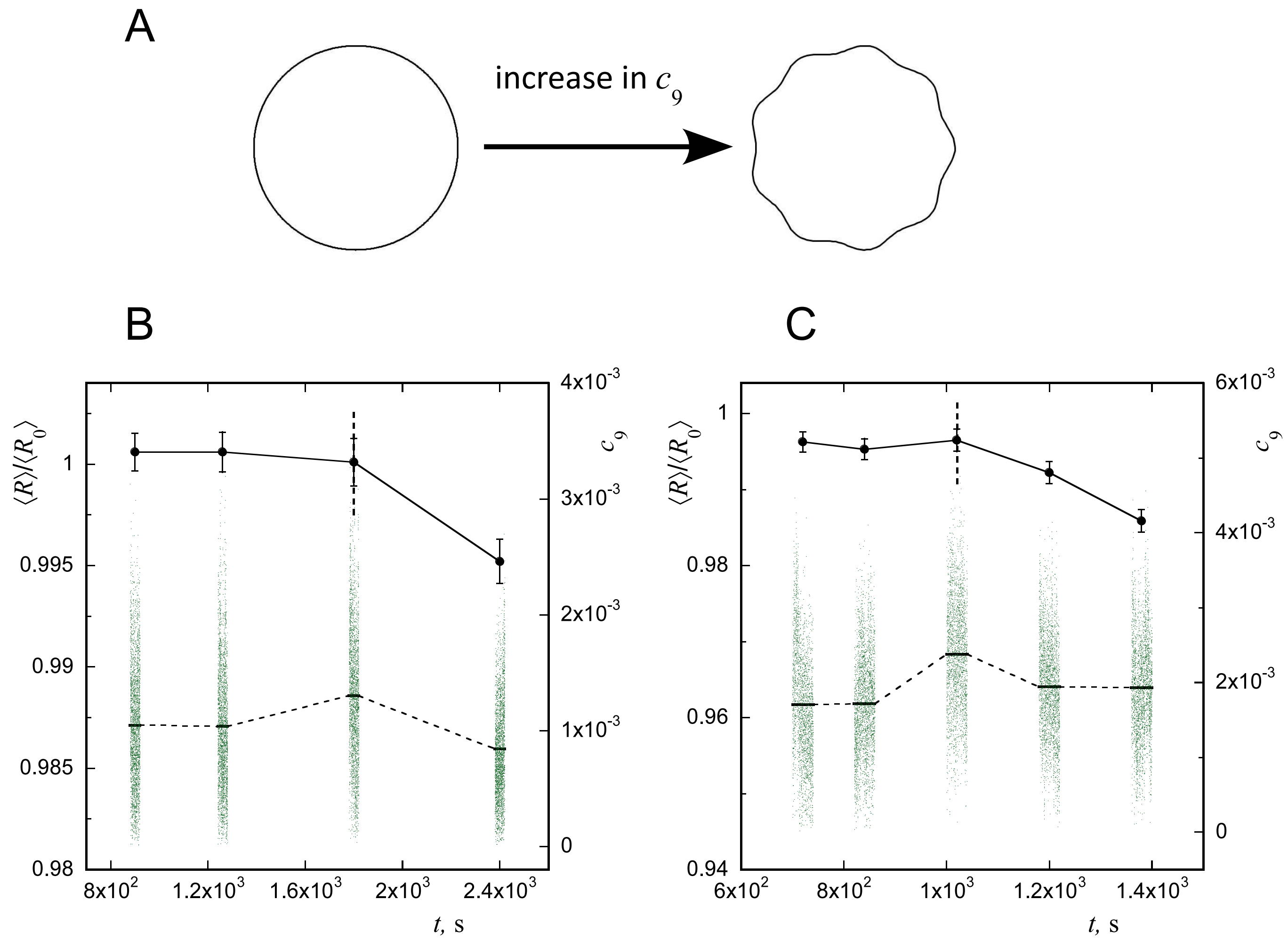
A
increase in c_9
B
$\langle R\rangle/\langle R_0\rangle$
c_9
1
0.995
0.99
0.985
0.98
4x10^-3
3x10^-3
2x10^-3
1x10^-3
0
8x10^2
1.2x10^3
1.6x10^3
2x10^3
2.4x10^3
t, s
C
$\langle R\rangle/\langle R_0\rangle$
c_9
1
0.98
0.96
0.94
6x10^-3
4x10^-3
2x10^-3
0
6x10^2
8x10^2
1x10^3
1.2x10^3
1.4x10^3
t, s

The interaction of α-toxin with lipid monolayers and bilayers leads to profound changes in the biophysical properties of the membrane.